HHS Public Access

Author manuscript

Curr Drug Targets. Author manuscript; available in PMC 2017 May 17.

Published in final edited form as:

Curr Drug Targets. 2015 ; 16(6): 571–581.

Opportunities for Photoacoustic-Guided Drug Delivery

Jun Xia[1,*], **Chulhong Kim**[2,*], and **Jonathan F. Lovell**[1,*]

[1]Department of Biomedical Engineering, University at Buffalo, Buffalo, USA

[2]Department of Creative IT Engineering, Pohang University of Science and Technology (POSTECH), Pohang, Republic of Korea

Abstract

Photoacoustic imaging (PAI) is rapidly becoming established as a viable imaging modality for small animal research, with promise of near-future human clinical translation. In this review, we discuss emerging prospects for photoacoustic-guided drug delivery. PAI presents opportunities for applications related to drug delivery, mainly with respect to either monitoring drug effects or monitoring drugs themselves. PAI is well-suited for imaging disease pathology and treatment response. Alternatively, PAI can be used to directly monitor the accumulation of various light-absorbing contrast agents or carriers with theranostic properties.

Keywords

Drug delivery; image-guided therapy; optoacoustic; photoacoustic; photothermal; theranostics

1. INTRODUCTION

1.1. A Brief Overview of PAI

There has been increasing interest in the use of photoacoustic imaging (PAI) for biomedical applications in the past decade. Similar to more established imaging modalities such as magnetic resonance imaging (MRI), X-ray computed tomography (CT), ultrasound imaging and others, PAI is capable of producing multi-dimensional images of both non-biological materials and biological tissues on basis of the photoacoustic (PA) phenomena. In 1880 Alexander Graham Bell first discovered the PA effect; the generation of sound waves induced by mechanically sliced sunlight, infrared light, or ultraviolet light [1, 2]. Later, Allen Rosencwaig at Bell Labs developed PA spectroscopic techniques for solid and biological samples in 1973 [3]. Buoyed by significant advances in laser and clinical ultrasound technology, biomedical applications of PAI were first introduced in 1990s. In 2003, the first *in vivo* non-invasive PA tomographic imaging of brain structures and functions was presented in rats by Wang *et al.*, and since then PAI technology has been extensively researched as a preclinical and clinical imaging modality [4].

*Address correspondence to: JX (junxia@buffalo.edu), CK (chulhong@postech.edu) or JFL (jflovell@buffalo.edu).

CONFLICT OF INTEREST

The authors declare no conflicts of interest in preparing this article.

When biological tissues are excited by pulsed light (typically on the order of nanoseconds), the light is absorbed by internal targets (Figure 1). These internal soft tissues expand due to the sudden temperature rise and consequently broadband acoustic waves are generated (referred to as PA waves). The initial PA amplitude can be expressed in equation (1) as follows:

$$p_0 = \Gamma \eta_{th} \mu_a F, \quad (1)$$

where Γ is the dimensionless Grueneisen coefficient, which is related to the target's temperature; η_{th} is the heat conversion efficiency (i.e., 1 minus the fluorescence quantum yield or the percentage of the nonradiative energy decay followed by laser excitation); μ_a is the optical absorption coefficient (cm^{-1}) which is directly linear to the concentration of the targeted chromophore; and F is the optical fluence (J/m^2). The product of μ_a and F can be stated as A_e, the specific optical absorption (i.e., energy deposition, J/m^3). Therefore, PAI is very sensitive to the optical absorption coefficients. It should also be noted that, to extract μ_a from p_0, the local fluence F needs to be quantified [5, 6]. The induced PA waves travel through the tissues and then are captured by a conventional ultrasound transducer. By measuring the times of arrivals of the PA waves, the depth-sensitive spatial information of the embedded targets can be extracted.

1.2. Types of implementation

PAI systems can be mainly implemented in two forms: (1) scanning-based photoacoustic microscopy (PAM) and (2) reconstruction-based photoacoustic computed tomography (PACT) [7]. The first type typically utilizes a single-element ultrasound transducer with mechanical raster or optical scanning to provide three-dimensional images. Scanning-based PAM can be further divided into two modes: (1) optical-resolution (OR) [8] and (2) acoustic-resolution (AR) PAM [9]. The typical penetration depth of OR-PAM is limited to one optical transport mean free path (i.e. ~ 1 mm), while that of AR-PAM can reach up to a few centimeters. The lateral resolution of OR-PAM is determined by optical hardware focusing (i.e., 0.51 λ_0/NA_o; λ_0, an optical wavelength; NA_o, the numerical aperture of the optical objective lens), while that of AR-PAM is derived by acoustic hardware focusing (i.e., $0.71\lambda_A/NA_A$; λ_A, a center acoustic wavelength; NA_A, the numerical aperture of the acoustic lens). The axial resolutions of both OR- and AR-PAM are determined by acoustic parameters (i.e., 0.88 $v_A/\Delta f_A$; v_A, the speed of ultrasound; Δf_A, the one-way bandwidth of the ultrasound transducer). The main advantage of scanning-based PAM over PACT is that it supplies superior image quality because hardware-based focusing does not pose any mathematical image reconstruction artifact and cross-talk does not exist among the transducer elements in an ultrasound array. The problem of scanning based PAM is relatively slow imaging acquisition due to the nature of raster scanning. Therefore, it takes tens of minutes to acquire one volumetric whole-body PA image of a small mouse. However, the imaging speed can be substantially enhanced by using a fast laser system.

PACT systems typically adapt ultrasound array probes such as a linear [10], arc, or full circular arrays [11]. Then, mathematical algorithms are applied to recover the final

tomographic PA images. Depending on the frequency of the transducer array, the penetration depth typically can be scalable from a few millimeters (i.e. above 10 MHz) to a few centimeters (i.e. 1–10 MHz). The main advantages of PACT include a real-time imaging capability and large field of view. Therefore, typical clinical PAI systems adapt this mode. The spatial resolution of PACT is the same as the axial resolution of scanning based PAM, 0.88 $v_A/\Delta f_A$. The key challenge of PACT is to improve image quality due to imperfect mathematical reconstruction algorithms.

1.3. Advantages and limitations

The main motivation of PAI is to provide strong intrinsic and extrinsic optical absorption contrast with high ultrasonic spatial resolution in deep tissues. The key benefits of PAI are summarized as follows: (1) PAI is a completely safe imaging modality because no ionizing radiation is involved. (2) The penetration depth can reach up to ~ 8 cm in biological tissues [12]. (3) Imaging depth and spatial resolution can be scaled by changing the ultrasonic frequency. (4) PA spectroscopy can distinguish a variety of chromophores. Intrinsic chromophores include oxy-hemoglobin, deoxy-hemoglobin, melanin, water, lipid, and so on. Extrinsic agents include organic dyes [13], organic nanoparticles [14], metallic nanoparticles [15], gold nanobeacons [16], carbon nanoparticles [17], polymeric nanoparticles [18], fluorescent proteins, and many others. (5) Inherently, PA images do not pose any speckle artifact. (6) PAI can be easily integrated with conventional pure optical and ultrasound imaging systems [19]. The main limitations of PAI are as follows: (1) the maximum penetration depth should not be beyond ~ 10 cm due to strong light attenuation in biological tissues. In an effort to overcome the depth-penetration limitation, different electromagnetic (EM) radiation sources have been explored, including radiofrequency waves [20], microwaves [21], and X-rays [22]. In this case, the signal origin comes from its corresponding EM wave absorption. (2) The best theoretical spatial resolution of PAI relies on the optical diffraction limit, a half of the optical wavelength. To further enhance the spatial resolution, nonlinear optical excitation can be applied.[23] (3) The following organs are difficult to be photoacoustically imaged using endogenous contrasts: the heart due to the position under the rib cage; the lungs due to the gas-tissue interface and the position under the rib cage; the stomach due to the hollow structure and the position under the rib cages; the bladder due to poor optical transparency; the pancreas due to its deep location; and bone due to acoustic attenuation and phase distortion.

1.4. Future applications

There have been some reports of using the photoacoustic effect for directly for controlling drug delivery. This has been show for delivering drugs to an arterial thrombus [24]. It is known that waves generated following laser propagate through tissue and can modulate properties such as permeability for drug delivery [25]. This method may have ramifications for transcutaneous drug delivery, although mechanical waves are thought to play a role, which are distinct from acoustic waves [26]. Drug delivery can be enhanced in the skin with photoacoustic and photomechanical waves [27]. However, the most promising approaches for PA drug delivery relate to imaging approaches.

PAI has been preclinically applied to study tumor angiogenesis/anti-angiogenesis, microcirculation, pharmacokinetics, drug delivery, disease treatment efficacy, brain physiology, tissue engineering, and pathology. Current and potential clinical applications include cancer diagnosis (i.e., melanoma [28], breast [29], prostate [30, 31], esophagus [32], and thyroid [33]), cancer staging [34], tracking needle biopsy [35], anesthesiology [36], cardiology using intravascular catheters[37], and transcranial imaging [38]. All these applications enforce the great potential of PAI for improving drug delivery.

2. MONITORING THE THERAPEUTIC EFFECT OF DRUGS

Capitalizing on a wide choice of endogenous and exogenous contrasts, PAI can derive a number of functional and molecular parameters of the tissue microenvironment, providing comprehensive information for diagnosis, staging, and treatment of diseases. In the following section, we review the parameters that can potentially be or have already been used for monitoring treatment efficacy. Representative images will be highlighted throughout the discussion.

2.1 Vasculature

Angiogenesis refers to the formation of new blood vessels, often within or surrounding a tumor, and is an essential indicator of disease progression. With high sensitivity to hemoglobin absorption, PAI is particularly powerful in vascular imaging. Compared with other vascular imaging modalities, such as X-ray CT, PAI has the unique capability of scaling its spatial resolution and imaging depth across both optical and ultrasonic dimensions, with spatial resolution ranging from a few microns (i.e., OR-PAM) to a hundred micron (i.e., AR-PAM and PACT) [39].

Using an OR-PAM system, Oladipupo *et al.* monitored angiogenesis in a transgenic mouse with continual epithelial HIF-1α induction from day 0 to day 14 [40]. With 2.56 μm spatial resolution, Figure 2a clearly shows a marked increase in microvessel density on day 14. After withdrawal of the angiogenic factor on day 15, a progressive reduction in vascular density can be observed, and by day 28 the overall density dropped by two-fold [40]. For deep-tissue vascular imaging using AR-PAM or PACT, the spatial resolution is not sufficient to resolve microvessels. However, PA amplitude is proportional to the total hemoglobin concentration within the resolution voxel, and can thus be used as an indirect measure of angiogenesis. Using a planar-view PACT system, Laufer *et al.* studied tumor vasculature and its response to a therapeutic vascular disrupting agent (OXi4503) [41]. The experiment was performed on a female nude mouse with human colorectal tumor xenografts (LS174T) implanted subcutaneously in the flank. An image acquired before the treatment shows strong signal in the tumor core, indicating angiogenesis (Figure 2b). 24 hours after intraperitoneal injection of the vascular disrupting agent, the PA amplitude in the tumor core was greatly reduced. At 48 hours post treatment, the tumor core showed a slight, diffusely distributed increase in signal intensity, indicating an accumulation of hemoglobin due to the reperfusion of vessels in the rim [41]. These two studies demonstrated that PAI can be used for monitoring the effect of drugs on angiogenesis at different spatial scales. PAI vascular imaging can also be enhanced by contrast agents. In a recent study, Nie *et al.* conjugated

Cyclic Arg-Gly-Asp to the surface of gold nanostars, creating a contrast agent for both sensitive angiography and photothermal therapy [42]. Gold nanobeacons have also been shown to be useful for angiogenesis imaging.[43]

Currently, multi-scale PAI vascular imaging is performed using different systems. With the introduction of optical-resolution PA computed microscopy (OR-PACM) [44], which achieves optical-resolution imaging in a PACT system, multi-scale vascular images can potentially be acquired using a single setup.

2.2 Hemodynamics

Beyond vascular imaging, PAI can also derive hemodynamic parameters, including the total concentration of hemoglobin (C_{Hb}), oxygen saturation (sO_2), blood flow, and metabolic rate of oxygen (MRO_2). C_{Hb} and sO_2 are commonly used to evaluate blood perfusion and oxygenation, respectively; blood flow is a strong indicator of cancer malignance, as tumor metabolism is often associated with an increased blood flow; and MRO_2 directly reflects the rate of oxygen consumption and is an ultimate measure of oxygen metabolism.

Because of its relatively shallow imaging depth, OR-PAM can easily perform hemodynamic imaging. C_{Hb} can be measured using isosbestic wavelengths of hemoglobin, such as 532 nm, 584 nm, and 794 nm, and the resulting PA signal amplitude directly reflects the C_{Hb} distribution, regardless of the oxygenation level. By adding one or two more wavelengths, the relative concentration of the two forms of hemoglobin (HbO_2 and HbR) can be quantified through spectral inversion. The speed of blood flow can be measured with a variety of methods, including Doppler frequency shift [45, 46], autocorrelation [47], and cross-correlation [48]. A high-speed OR-PAM system even allows direct visualization of flowing red blood cells [49]. Hence, OR-PAM is able to measure all the parameters required to quantify MRO_2. Combining all these parameters, Yao *et al.* studied hemodynamic responses to cryotherapy, which was introduced by placing a 1-mm diameter cryo-probe on a mouse ear for 10 s (Figure 3) [50]. Right after the treatment, a global reflective vasodilatation was observed, which was accompanied by an increase in blood flow and a decrease in oxygen extraction fraction (OEF). MRO_2 remained unchanged in the control (untreated) area and decreased by more than 50% in the treated area, due to the cryotherapy-induced cell death. Over 30 days following treatment, all the hemodynamic parameters in the control area recovered almost monotonically to the baseline. In the treated area, the physiological progress was more complicated. In the first three days, the blood flow and OEF trended toward the baseline, while MRO_2 remained at a low level due to cell necrosis. Starting from day five, inflammation was observed, followed by increases in flow speed and MRO_2, as well as a decrease in OEF, reflecting improved tissue viability [50]. By day 30, all the hemodynamic parameters had recovered almost to the baseline. This extended study shows that OR-PAM allows comprehensive monitoring of different physiological phases of therapeutic regimes.

Because of the unknown fluence distribution, quantifying hemodynamic parameters in deep tissue is more challenging [5]. Nevertheless, encouraging progress has been made in the past few years to address this issue. For C_{Hb} and sO_2 quantification, PACT has been combined with other optical tomography modalities, such as Diffusive Optical Tomography (DOT), to

correct for heterogeneities in light fluence distributions [51, 52]. Advanced data processing algorithms, such as acoustic spectral analysis [53] and dynamic sO_2 calculation [54], have also been proposed to circumvent the unknown fluence, providing calibration-free quantification of sO_2. For flow measurement, Wang *et al.* [55] developed a novel approach that thermally tagged the flowing medium using a HIFU (high-intensity focused ultrasound) transducer. Because the PA amplitude is proportional to the temperature of the object, their method allows direct visualization of flowing blood in deep tissues. With these advances, PACT promises to provide comprehensive deep-tissue hemodynamic monitoring for treatment evaluation. PACT has been used to monitor vascular shutdown in response to photodynamic therapy [56]. As we will discuss later, PA approaches have also been used to monitor photodynamic therapy agents themselves.

2.3 Functional connectivity

Resting-state functional connectivity imaging is an emerging neural research approach that has great potential in evaluating the efficiency of brain disease treatments [57–59]. Recent studies found that, in a healthy brain, resting-state hemodynamic fluctuations correlated inter-hemispherically between bilaterally homologous regions, as well as intra-hemispherically within the same functional regions. In patients with brain disorders, such as Alzheimer's, correlation between certain regions was found to be greatly reduced. The task-free nature of resting-state imaging makes it an appealing approach for animal studies.

Using a full-ring array PACT system, Nasiriavanaki *et al.* reported the first high-resolution functional connectivity imaging of a mouse brain [60]. A unique advantage of PACT is that the functional connectivity maps are automatically co-registered with high-resolution cortical vascular images, allowing the exact pinpointing of the location of neural processes. To extract the resting-state signal, the reconstructed temporal PA images were processed through spatial smoothing, mean pixel value subtraction, temporal filtering (to the functional connectivity frequency band), and global regression. A parcellation algorithm was then used to generate the functional divisions of the brain in a data-driven manner [60]. Because the experiment was performed on a healthy mouse, the resulting parcellation map (Figure 4a) agreed well with the standard functional brain atlas (Figure 4b). This study indicates that functional connectivity PACT can be used as a noninvasive tool for the diagnosis and therapeutic monitoring of neurological diseases.

2.4 Melanoma

While PAI is applicable for general monitoring of cancers [61], PAI is particularly well-suited for imaging pigmented lesions [28]. For melanoma, the depth of the tumor (Breslow's thickness), measured from the top of the epidermis, is the most important prognostic indicator determining the propensity to metastasis. As PAI is sensitive to absorptions from both hemoglobin and melanin, it has great potential to exceed the current gold standard (Breslow's thickness) by providing three-dimensional information of the entire tumor [28].

Among various PAI implementations, AR-PAM and planar-view PACT, which image the tissue from above, are the best suited for melanoma imaging in either animals [62] or humans [63]. In 2006, Zhang *et al.* demonstrated the first 3D morphology of both melanoma

and surrounding blood vessels on a nude mouse with subcutaneously inoculated B16-melanoma (Figure 5) [62]. To separate the absorptions of hemoglobin and melanin, the experiment was performed using two wavelengths — 584 nm and 764 nm. In Figure 5a, microvessels with diameters of less than a single pixel are seen to surround the melanoma, indicating angiogenesis [62]. The depth of the tumor can be obtained by sectioning the volumetric data along arbitrary directions. The cross-sectional image in Figure 5c agrees well with the corresponding histological result (Figure 5c), indicating that PAI can potentially minimize the need for biopsies. Combining hemodynamic and structural information, PAI will greatly improve the treatment planning and evaluation of melanoma.

2.5 Temperature

PA amplitude is sensitive to the Grüneisen coefficient, which is a measure of the thermo-mechanical conversion efficiency, and the coefficient increases as the tissue temperature rises. Thus PAI can be used to noninvasively map the tissue's temperature distribution, which is particularly useful in monitoring thermotherapy [65, 66]. Because of the unknown local fluence, a baseline image needs to be acquired prior to the therapy. Subsequent changes in PA amplitude measured during thermotherapy can then be used to derive the absolute temperature rise. As the Grüneisen coefficient varies almost linearly with the temperature, a 1% increase in PA signal implies a 0.37 ºC change in temperature (assuming a baseline tissue temperature of 37 ºC) [55]. Thus the thermal dose during thermotherapy could be monitored and adjusted in real-time. This approach was also used to monitor heating induced by hollow gold nanoshells using PAI [67].

2.6 Molecular imaging

Molecular imaging allows direct visualization of cellular functions and molecular processes, and it plays a key role in the diagnosis and treatment of diseases. By using various exogenous contrast agents, including microbubbles [68–70], organic dyes [64, 71], nanoparticles [18, 72], fluorescent proteins [73–75], and reporter gene products [76], PAI provided high sensitivity molecular imaging. For example, one interesting demonstration of molecular PAT was imaging tumor glucose metabolism. While 18-fluorodeoxyglucose positron emission tomography (FDG-PET) is the current standard for tumor metabolism evaluation, it cannot provide anatomical information. Thus FDG-PET needs to be combined MRI or X-ray CT to pinpoint the location of a hyper-metabolic site. Combining endogenous (hemoglobin) and exogenous (IRDye800-2DG) PA contrasts, Chatni *et al.* demonstrated simultaneous anatomical and glucose metabolic imaging in a full-ring array PACT system [64]. The experiment was performed in mice with orthotopically implanted 786-O kidney tumor cells. A representative cross-sectional image is presented in Figure 5d. The anatomical image (gray) shows that the cancerous kidney (left) is much larger than the healthy kidney (right), and the superposed metabolic image (color) indicates the hyper-metabolic site on the cancerous kidney. Using a different fluorescent dye, 2NBDG, which has a smaller molecular size, Yao *et al.* demonstrated imaging of brain metabolism *in vivo* [77]. Thus PAI can potentially be used to monitor glucose metabolism for cancer therapy.

As with hemodynamic imaging, deep-tissue molecular imaging is also affected by unknown fluence. For accurate spectrum separation, the contrast of interest should have an absorption

spectrum distinct from those of surrounding tissues [6]. For instance, the absorption spectrum of the IRDye800-2DG used in [64] peaks at 776 nm, where absorptions from the two forms of hemoglobin are relatively weak. To further increase the accuracy of spectrum separation and subsequently improve the specificity of molecular PAI, novel contrast agents are needed. In a recent report, Jin *et al.* developed a magnetic contrast agent which can be trapped and spatially modulated by a magnetic field [78], allowing the contrast signal to be accurately extracted from surrounding tissue. With continuing efforts in contrast agent development, molecular PAI will play a key role in therapeutic planning and monitoring.

Another interesting approach to contrast-based functional imaging involves monitoring of the intestine. Naphthalocyanine dyes self-assembled with block copolymers in frozen micelles have been shown to give rise to nanoparticulate solutions with exceptionally high NIR absorptions values for high-contrast PAI [79]. These pass safely and quantitatively through the intestine into feces. PAI was used to monitor intestine anatomy, function (the rate of peristalsis) and acute conditions (obstruction). Using this approach, the effect of drugs of on gastrointestinal conditions may be monitored directly. Figure 6 shows real-time PAI monitoring of peristalsis.

3. MONITORING DRUGS THEMSELVES

3.1 Monitoring the distribution of therapeutics

In addition to using PAI for monitoring therapeutic response of drugs by examining functional and molecular parameters as outlined in in the previous section, PAI holds intriguing potential for non-invasively monitoring parameters such as drug biodistribution, pharmacokinetics, and delivery to target tissue. Since PA imaging of biological systems contrast is most effective in the NIR wavelength range, NIR-absorbing compounds have the most applicability for drug monitoring. Unfortunately, with the exception of photosensitizers used in photodynamic therapy, few if any clinically-used medicinal compounds have strong intrinsic optical absorption in the NIR. Recent years have seen a large expansion in pre-clinical photothermal therapy (PTT), which often make use of novel NIR contrast agents and is a naturally-suited pairing with PAI. These photothermal contrast agents are theranostic, since they can be applied for both imaging as well as therapeutic photomedicine techniques [80].

Numerous carriers have capability for PA monitoring as well as drug delivery including carbon nanotubes[81], gold nanoparticles[82], and porphysomes[83]. By loading conventional drugs into nanocarriers that have strong NIR absorption, the nanocarrier can be non-invasively imaged and assessed as an indirect proxy for drug biodistribution, as shown in Figure 7. Rather than using NIR-active nanocarriers, an alternate approach could be to co-load drugs of interest with small molecule NIR dyes into a common carrier. A commonly used NIR-absorbing molecule such as indocyanine green is appropriate and can readily be loaded into nanoparticles that also possess drug-loading capability [84, 85]. The limitations of these approaches are that in many cases, the drug may dissociate from the nanocarrier or co-loaded contrast agent. Therefore, stability of the drug and NIR carrier or co-loaded dye should be thoroughly characterized. Another consideration is that nanocarriers that have NIR absorption are not currently in clinical use and studying drug delivery using carriers that

may never be approved for human use seems less than ideal. For strategies that involve NIR chromophores and co-loading, the act of co-loading may itself modulate the stability and behavior of the actual drug of interest. Despite these drawbacks, the potential advantages of non-invasively monitoring drug pharmacokinetics, biodistribution and accumulation in the target tissue at user-defined variable resolutions using portable and modular PAI systems are compelling. In preclinical pharmacokinetic studies, instead of having to sacrifice animals at multiple time points to determine biodistribution, non-invasive monitoring would enable a much smaller and more manageable number subjects to be used. This could increase the pace and breadth of scientific discovery. However, to our knowledge, few studies have been reported that have used PAI for examination of the pharmacokinetic and biodistribution parameters of drugs loaded onto NIR-active nanocarriers or co-loaded with NIR-active dyes. There have been recent examples of using PAI for examining pharmacokinetic properties of dyes in contexts such as gastric emptying time [86], and such approaches are expected to be extended to drug delivery applications.

3.2 Photothermal contrast agents

Photothermal contrast agents are particularly well-suited for PA methods. Localized thermal ablation techniques, such as radiofrequency ablation have been known for over a century and have been used clinically for several decades, particularly for treating liver cancers [87]. Laser-mediated photothermal tissue ablation without the use of contrast-agents has been explored for over twenty years [88]. However, the introduction of photothermal contrast agents, many of which have been in the form of nanoparticles, has greatly expanded research interests in PTT in the past decade. The clinical potential of PTT using nanoparticle-enabled therapies has been noted [89], but successful clinical translation remains a challenge, with few successes in humans reported. By using nanoparticulate contrast agents that can selectively be retained in a tumor, through the enhanced permeability and retention effect or through active targeting, lower laser power and deeper light penetration can be used and tissue damage can contained to selectively heats and destroy the tumor. Concurrent with the recent interest in PTT agents, PA contrast agents have similarly grown in interest, often using the same agents for either modality [90, 91]. Since both rely on photothermal conversion efficiency, PAT and PTT agents can be used synergistically for directly observing the contrast agent accumulation in the tumor using PAT prior to PTT. PAT could be used for monitoring the extent to which the NIR contrast is localized, thus enabling treatment planning for ensuring proper light delivery to destroy the target tissue and to avoid overheating important adjacent tissues. Several inorganic and organic nanoparticles have been used for PTT and PAT purposes and been reviewed extensively [90, 92–94]. We will mention only a few representative examples here.

The dominant class of nanoparticle used for PAI and PTT has been gold-based plasmonic nanoparticles. Gold plasmonic nanoparticles have intriguing optical and electronic properties since their delocalized electrons undergo a collective oscillation known as surface plasmon resonance when interacting with particular electromagnetic radiation wavelengths. They can strongly absorb and scatter visible and NIR light in such a way that highly relates nanoparticle size and shape to light absorption [95]. In 2003, gold nanoshells, which consist of a dialectric silica core surrounded by a thin plasmonic gold layer, were demonstrated to

be useful for photothermal ablation of tumors following intratumoral administration [96]. The following year, gold nanoshells were demonstrated for use as contrast agents for PAT following systemic administration in a brain imaging study [97]. These studies, in which a single type of plasmonic nanoparticle was used for both PAI and PAT, are now over a decade old and helped fuel a vast number of follow-up studies that made use of various types of gold NIR plasmonic materials [98].

Hollow gold nanospheres, which are similar to gold nanoshells but lack the silica core, have been used for multimodal PAI and PTT [99]. In this elegant study, PAI was used to first assess the delivery of hollow nanospheres targeted to integrins that were overexpressed in blood vessels in a mouse model of glioma. Mice were then treated with a near-infrared laser for PTT, which elevated tumor temperature by over 20 °C for effective tumor ablation that significantly prolonged the survival of tumor-bearing mice.

Gold nanorods are commercially available, have amongst the highest near infrared absorption cross-sections and have been used extensively in PAI and PTT [100]. By using antibodies, gold nanorods could be targeted to surface receptors on cancer cells for enhanced PA detection based on molecular imaging [101]. PEGylated nanorods have been used for effective image-guided PTT [102]. Although in that case the imaging modality was X-ray CT, the same principle could be applied to PAI. It has further been shown that by coating gold nanorods with a silica layer, a PA amplification signal can be obtained [103].

While gold nanorods and nanoshells have been perhaps the most commonly used inorganic nanoparticles for applications with pertinence to PA-guided theranostics, many others are worth noting. Gold nanocages, which are small porous structures with thin walls, have been used for PAI, PTT, and also have been engineered to directly release drugs in response to laser light [104]. Gold nanohexapods are a newer class of plasmonic gold nanoparticle with six legs and have been shown to compare favorably to nanocages and nanorods for photothermal treatments [105]. Besides gold-based plasmonic materials, carbon nanotubes have been frequently-used as a versatile PAI contrast agents [106]. Carbon nanotubes are well-suited for photothermal therapy [107] as well as drug-delivery [108]. More recently, the related carbon-based material of nanographene has shown similar versatility for theranostic NIR applications [109]. Other NIR-active inorganic materials that have been garnering interest lately include molybdenum disulfide [110] and copper sulfide [111] nanoparticles.

Organic materials, by definition, tend to have less associated concerns about fundamental incompatibility in the body compared to inorganic materials. Traditionally, most biocompatible organic nanoparticles have not had strong NIR character. However, in recent years there has been a large number of organic nanoparticles developed with excellent potential for PTT and PAI. Porphyrin-based materials are well-suited for theranostic applications and have NIR character [112]. One example is porphysomes, which are liposome-like particles formed from a densely-packed porphyrin bilayer which is biodegradable[113], have been shown to be useful for PAI and PTT [14] as well as light-triggered drug release applications [114]. Porphysomes were used to demonstrate that PTT, but not photodynamic therapy, can destroy hypoxic tumors [115]. Conductive polymer

nanoparticles have also been shown to have excellent potential for both PTT [116, 117] and PAI [18].

3.3 Photodynamic therapy agents

Photodynamic therapy is clinically-used localized technique that involves toxic singlet oxygen generation by a systemically administered photosensitizer in response to applied laser light [118, 119]. Because NIR light can penetrate human tissue most effectively, photosensitizers have been selected that exhibit strong absorption in the NIR, which matches the desired properties of a PAI agent. Common photosensitizers exhibit PA contrast and can be useful for PAI imaging in vivo [120]. This study showed that a photosensitizer localization could be visualized in the tumor 10 minutes post injection and reached peak accumulation after an hour and was cleared within 24 hours, thus, demonstrating the potential of PAI to non-invasively monitor drug delivery and guide treatment strategy.

Although photosensitizers have good NIR absorption, because they generate superstoichiometric quantities of singlet oxygen, they may not necessarily accumulate in high enough quantity for PA detection. Another noteworthy approach that has been used recently is to combine photosensitizers with NIR-absorbing nanoparticle to enhance detection. Chlorin e6 was used to functionalize gold nanostars and this combination agent was used for combined PDT and PTT [121]. In another example, hematoporphyrin was loaded onto gold nanorods for an enhanced combination phototherapy effect [122]. The photosensitizer HPPH was loaded onto gold nanocages and used for PAI in addition to enhanced photodynamic therapy [123].

4. CONCLUSION

In summary, PAI has been evolving rapidly in the past decade and continues to see substantial refinement and expansion of capabilities. Like other imaging modalities, functional imaging is a central advantageous feature of PAI. This enables monitoring of drug response based on a wide variety of measurements including vasculature response, hemodynamics, neuron connectivity, melanoma tracking, and local temperature. Use of molecular imaging probes further expands those capabilities. PAI may also be used for direct monitoring of drugs that use make use NIR-active carriers or dyes or that themselves have NIR character as is the case for PTT and PDT agents. Drug delivery methodologies stand to greatly benefit from new PAI techniques.

Acknowledgments

This work was supported by the National Institutes of Health (R01EB017270), and the Korean Ministry of Science, ICT and Future Planning (IT Consilience Creative Program; NIPA-2013-H0203-13-1001 and NRF-2011-0030075).

References

1. Bell AG. The Production of Sound by Radiant Energy. Science. 1881; 2(49):242–53.
2. Bell AG. The Photophone. Science. 1880; 1(11):130–4.
3. Rosencwaig A. Photoacoustic spectroscopy of biological materials. Science. 1973; 181(4100):657–8. [PubMed: 4353357]

4. Wang X, Pang Y, Ku G, Xie X, Stoica G, Wang LV. Noninvasive laser-induced photoacoustic tomography for structural and functional in vivo imaging of the brain. Nat Biotechnol. 2003; 21(7): 803–6. [PubMed: 12808463]
5. Cox B, Laufer JG, Arridge SR, Beard PC. Quantitative spectroscopic photoacoustic imaging: a review. J Biomed Opt. 2012; 17(6):061202–1. [PubMed: 22734732]
6. Beard P. Biomedical photoacoustic imaging. Interface Focus. 2011; 1(4):602–631. [PubMed: 22866233]
7. Wang LV, Hu S. Photoacoustic tomography: in vivo imaging from organelles to organs. Science. 2012; 335(6075):1458–62. [PubMed: 22442475]
8. Kim C, Park S, Kim J, et al. Objective-free optical-resolution photoacoustic microscopy. J Biomed Opt. 2013; 18(1):10501. [PubMed: 23232814]
9. Kim C, Jeon M, Wang LV. Nonionizing photoacoustic cystography in vivo. Opt Lett. 2011; 36(18): 3599–601. [PubMed: 21931403]
10. Kim C, Erpelding TN, Jankovic L, Wang LV. Performance benchmarks of an array-based hand-held photoacoustic probe adapted from a clinical ultrasound system for non-invasive sentinel lymph node imaging. Philos Trans A Math Phys Eng Sci. 2011; 369(1955):4644–50. [PubMed: 22006911]
11. Xia J, Chatni MR, Maslov K, et al. Whole-body ring-shaped confocal photoacoustic computed tomography of small animals in vivo. J Biomed Opt. 2012; 17(5):050506. [PubMed: 22612121]
12. Ke H, Erpelding TN, Jankovic L, Liu C, Wang LV. Performance characterization of an integrated ultrasound, photoacoustic, and thermoacoustic imaging system. J Biomed Opt. 2012; 17(5): 056010. [PubMed: 22612133]
13. Kim C, Song KH, Gao F, Wang LV. Sentinel lymph nodes and lymphatic vessels: noninvasive dual-modality in vivo mapping by using indocyanine green in rats--volumetric spectroscopic photoacoustic imaging and planar fluorescence imaging. Radiology. 2010; 255(2):442–50. [PubMed: 20413757]
14. Lovell JF, Jin CS, Huynh E, et al. Porphysome nanovesicles generated by porphyrin bilayers for use as multimodal biophotonic contrast agents. Nat Mater. 2011; 10(4):324–32. [PubMed: 21423187]
15. Kim C, Cho EC, Chen J, et al. In vivo molecular photoacoustic tomography of melanomas targeted by bioconjugated gold nanocages. ACS Nano. 2010; 4(8):4559–64. [PubMed: 20731439]
16. Pan D, Pramanik M, Senpan A, et al. Molecular photoacoustic tomography with colloidal nanobeacons. Angew Chem Int Ed. 2009; 48(23):4170–3.
17. Koo J, Jeon M, Oh Y, et al. In vivo non-ionizing photoacoustic mapping of sentinel lymph nodes and bladders with ICG-enhanced carbon nanotubes. Phys Med Biol. 2012; 57(23):7853–62. [PubMed: 23151772]
18. Pu K, Shuhendler AJ, Jokerst JV, et al. Semiconducting polymer nanoparticles as photoacoustic molecular imaging probes in living mice. Nat Nanotechnol. 2014; 9(3):233–9. [PubMed: 24463363]
19. Jeon M, Kim C. Multimodal Photoacoustic Tomography. IEEE Trans Multimedia. 2013; 15(5): 975–982.
20. Kruger RA, Kopecky KK, Aisen AM, Reinecke DR, Kruger GA, Kiser WL. Thermoacoustic CT with Radio Waves: A Medical Imaging Paradigm. Radiology. 1999; 211(1):275–278. [PubMed: 10189483]
21. Ku G, Wang LV. Scanning microwave-induced thermoacoustic tomography: Signal, resolution, and contrast. Med Phys. 2001; 28(1):4–10. [PubMed: 11213921]
22. Xiang L, Han B, Carpenter C, Pratx G, Kuang Y, Xing L. X-ray acoustic computed tomography with pulsed x-ray beam from a medical linear accelerator. Med Phys. 2013; 40(1)
23. Yao J, Wang L, Li C, Zhang C, Wang LV. Photoimprint photoacoustic microscopy for three-dimensional label-free subdiffraction imaging. Phys Rev Lett. 2014; 112(1):014302. [PubMed: 24483902]
24. Gregory KW, Shearin A, Prahl SA. Photoacoustic drug delivery to arterial thrombus - A new method for local drug delivery. Circulation. 1996; 94(8):1166–1166.

25. Doukas AG, Flotte TJ. Physical characteristics and biological effects of laser-induced stress waves. Ultrasound Med Biol. 1996; 22(2):151–64. [PubMed: 8735525]
26. Lee S, McAuliffe DJ, Flotte TJ, Kollias N, Doukas AG. Photomechanical transcutaneous delivery of macromolecules. J Invest Dermatol. 1998; 111(6):925–9. [PubMed: 9856797]
27. Lee S, Kollias N, McAuliffe DJ, Flotte TJ, Doukas AG. Topical drug delivery in humans with a single photomechanical wave. Pharm Res. 1999; 16(11):1717–21. [PubMed: 10571277]
28. Favazza CP, Jassim O, Cornelius LA, Wang LHV. In vivo photoacoustic microscopy of human cutaneous microvasculature and a nevus. J Biomed Opt. 2011; 16(1)
29. Kruger RA, Kuzmiak CM, Lam RB, Reinecke DR, Del Rio SP, Steed D. Dedicated 3D photoacoustic breast imaging. Med Phys. 2013; 40(11)
30. Harrison T, Zemp RJ. Coregistered photoacoustic-ultrasound imaging applied to brachytherapy. J Biomed Opt. 2011; 16(8):080502. [PubMed: 21895302]
31. Su JL, Bouchard RR, Karpiouk AB, Hazle JD, Emelianov SY. Photoacoustic imaging of prostate brachytherapy seeds. Biomed Opt Express. 2011; 2(8):2243–2254. [PubMed: 21833361]
32. Yang JM, Favazza C, Chen RM, et al. Simultaneous functional photoacoustic and ultrasonic endoscopy of internal organs in vivo. Nat Med. 2012; 18(8):1297–1302. [PubMed: 22797808]
33. Levi J, Kothapalli SR, Bohndiek S, et al. Molecular Photoacoustic Imaging of Follicular Thyroid Carcinoma. Clin Cancer Res. 2013; 19(6):1494–1502. [PubMed: 23349314]
34. Erpelding TN, Kim C, Pramanik M, et al. Sentinel Lymph Nodes in the Rat: Noninvasive Photoacoustic and US Imaging with a Clinical US System. Radiology. 2010; 256(1):102–110. [PubMed: 20574088]
35. Kim C, Erpelding TN, Maslov K, et al. Handheld array-based photoacoustic probe for guiding needle biopsy of sentinel lymph nodes. J Biomed Opt. 2010; 15(4):046010-046010–4. [PubMed: 20799812]
36. Abenstein JP, Welna JO. Clinical evaluation of a photoacoustic cas analyzer. Anesthesiology. 1991; 75(3):A463.
37. Sethuraman S, Aglyamov SR, Amirian JH, Smalling RW, Emelianov SY. Intravascular photoacoustic imaging using an IVUS imaging catheter. IEEE Trans Ultrason Ferroelectr Freq Control. 2007; 54(5):978–986. [PubMed: 17523562]
38. Nie L, Cai X, Maslov K, Garcia-Uribe A, Anastasio MA, Wang LV. Photoacoustic tomography through a whole adult human skull with a photon recycler. J Biomed Opt. 2012; 17(11):110506–110506. [PubMed: 23123972]
39. Wang LV, Hu S. Photoacoustic Tomography: In Vivo Imaging from Organelles to Organs. Science. 2012; 335(6075):1458–1462. [PubMed: 22442475]
40. Oladipupo SS, Hu S, Santeford AC, et al. Conditional HIF-1 induction produces multistage neovascularization with stage-specific sensitivity to VEGFR inhibitors and myeloid cell independence. Blood. 2011; 117(15):4142–4153. [PubMed: 21307392]
41. Laufer J, Johnson P, Zhang E, et al. In vivo preclinical photoacoustic imaging of tumor vasculature development and therapy. J Biomed Opt. 2012; 17(5)
42. Nie LM, Wang SJ, Wang XY, et al. In Vivo Volumetric Photoacoustic Molecular Angiography and Therapeutic Monitoring with Targeted Plasmonic Nanostars. Small. 2014; 10(8):1585–1593. [PubMed: 24150920]
43. Pan D, Pramanik M, Senpan A, et al. Molecular photoacoustic imaging of angiogenesis with integrin-targeted gold nanobeacons. FASEB J. 2011; 25(3):875–82. [PubMed: 21097518]
44. Xia J, Li G, Wang L, et al. Wide-field two-dimensional multifocal optical-resolution photoacoustic-computed microscopy. Opt Lett. 2013; 38(24):5236–5239. [PubMed: 24322226]
45. Fang H, Maslov K, Wang LV. Photoacoustic Doppler flow measurement in optically scattering media. Appl Phys Lett. 2007; 91(26):264103.
46. Yao J, Wang LV. Transverse flow imaging based on photoacoustic Doppler bandwidth broadening. J Biomed Opt. 2010; 15(2):021304. [PubMed: 20459226]
47. Chen SL, Ling T, Huang SW, Baac HW, Chang YC, Guo LJ. Photoacoustic correlation technique for low-speed flow measurement. Proc Society Photo-Opt Instr Eng. 2010; 7564(1):75642I.

48. Brunker J, Beard P. Pulsed photoacoustic Doppler flowmetry using time-domain cross-correlation: accuracy, resolution and scalability. J Acoust Soc Am. 2012; 132(3):1780–91. [PubMed: 22978905]
49. Wang L, Maslov K, Wang LV. Single-cell label-free photoacoustic flowoxigraphy in vivo. Proc Natl Acad Sci U S A. 2013; 110(15):5759–64. [PubMed: 23536296]
50. Yao J, Maslov KI, Zhang Y, Xia Y, Wang LV. Label-free oxygen-metabolic photoacoustic microscopy in vivo. J Biomed Opt. 2011; 16(7):076003. [PubMed: 21806264]
51. Bauer AQ, Nothdurft RE, Erpelding TN, Wang LV, Culver JP. Quantitative photoacoustic imaging: correcting for heterogeneous light fluence distributions using diffuse optical tomography. J Biomed Opt. 2011; 16(9):096016. [PubMed: 21950930]
52. Li XQ, Xi L, Jiang RX, Yao L, Jiang HB. Integrated diffuse optical tomography and photoacoustic tomography: phantom validations. Biomed Opt Express. 2011; 2(8):2348–2353. [PubMed: 21833371]
53. Guo Z, Favazza C, Garcia-Uribe A, Wang LV. Quantitative photoacoustic microscopy of optical absorption coefficients from acoustic spectra in the optical diffusive regime. J Biomed Opt. 2012; 17(6):066011–1. [PubMed: 22734767]
54. Xia J, Danielli A, Liu Y, Wang L, Maslov K, Wang LV. Calibration-free quantification of absolute oxygen saturation based on the dynamics of photoacoustic signals. Opt Lett. 2013; 38(15):2800–2803. [PubMed: 23903146]
55. Wang L, Xia J, Yao J, Maslov KI, Wang LV. Ultrasonically Encoded Photoacoustic Flowgraphy in Biological Tissue. Phys Rev Lett. 2013; 111(20):204301. [PubMed: 24289689]
56. Xiang L, Xing D, Gu H, et al. Real-time optoacoustic monitoring of vascular damage during photodynamic therapy treatment of tumor. J Biomed Opt. 2007; 12(1):014001. [PubMed: 17343476]
57. Deco G, Jirsa VK, McIntosh AR. Emerging concepts for the dynamical organization of resting-state activity in the brain. Nat Rev Neurosci. 2011; 12(1):43–56. [PubMed: 21170073]
58. Fox MD, Raichle ME. Spontaneous fluctuations in brain activity observed with functional magnetic resonance imaging. Nat Rev Neurosci. 2007; 8(9):700–711. [PubMed: 17704812]
59. Buckner RL, Krienen FM, Yeo BTT. Opportunities and limitations of intrinsic functional connectivity MRI. Nat Neurosci. 2013; 16(7):832–837. [PubMed: 23799476]
60. Nasiriavanaki M, Xia J, Wan H, Bauer AQ, Culver JP, Wang LV. High-resolution photoacoustic tomography of resting-state functional connectivity in the mouse brain. Proc Natl Acad Sci U S A. 2014; 111(1):21–6. [PubMed: 24367107]
61. Mehrmohammadi M, Yoon SJ, Yeager D, Emelianov SY. Photoacoustic Imaging for Cancer Detection and Staging. Curr Mol Imaging. 2013; 2(1):89–105. [PubMed: 24032095]
62. Zhang HF, Maslov K, Stoica G, Wang LV. Functional photoacoustic microscopy for high-resolution and noninvasive in vivo imaging. Nat Biotech. 2006; 24(7):848–851.
63. Favazza CP, Cornelius LA, Wang LHV. In vivo functional photoacoustic microscopy of cutaneous microvasculature in human skin. J Biomed Opt. 2011; 16(2)
64. Chatni MR, Xia J, Sohn R, et al. Tumor glucose metabolism imaged in vivo in small animals with whole-body photoacoustic computed tomography. J Biomed Opt. 2012; 17(7):076012. [PubMed: 22894495]
65. Shah J, Park S, Aglyamov S, et al. Photoacoustic imaging and temperature measurement for photothermal cancer therapy. J Biomed Opt. 2008; 13(3)
66. Pramanik M, Wang LV. Thermoacoustic and photoacoustic sensing of temperature. J Biomed Opt. 2009; 14(5)
67. Lee HJ, Liu Y, Zhao J, et al. In vitro and in vivo mapping of drug release after laser ablation thermal therapy with doxorubicin-loaded hollow gold nanoshells using fluorescence and photoacoustic imaging. J Control Release. 2013; 172(1):152–8. [PubMed: 23920038]
68. Kim C, Qin RG, Xu JS, Wang LV, Xu R. Multifunctional microbubbles and nanobubbles for photoacoustic and ultrasound imaging. J Biomed Opt. 2010; 15(1)
69. Jeon M, Song WT, Huynh E, et al. Methylene blue microbubbles as a model dual-modality contrast agent for ultrasound and activatable photoacoustic imaging. J Biomed Opt. 2014; 19(1)

70. Huynh E, Lovell JF, Helfield BL, et al. Porphyrin shell microbubbles with intrinsic ultrasound and photoacoustic properties. J Am Chem Soc. 2012; 134(40):16464–7. [PubMed: 22827774]
71. Li M-L, Jung-Taek O, Xueyi X, et al. Simultaneous Molecular and Hypoxia Imaging of Brain Tumors In Vivo Using Spectroscopic Photoacoustic Tomography. Proceedings of the IEEE. 2008; 96(3):481–489.
72. Kircher MF, de la Zerda A, Jokerst JV, et al. A brain tumor molecular imaging strategy using a new triple-modality MRI-photoacoustic-Raman nanoparticle. Nat Med. 2012; 18(5):829–834. [PubMed: 22504484]
73. Filonov GS, Krumholz A, Xia J, Yao J, Wang LV, Verkhusha VV. Deep-Tissue Photoacoustic Tomography of a Genetically Encoded Near-Infrared Fluorescent Probe. Angewandte Chemie International Edition. 2012; 51(6):1448–1451. [PubMed: 22213541]
74. Krumholz A, Shcherbakova DM, Xia J, Wang LV, Verkhusha VV. Multicontrast photoacoustic in vivo imaging using near-infrared fluorescent proteins. Sci Rep. 2014; 4:3939. [PubMed: 24487319]
75. Razansky D, Distel M, Vinegoni C, et al. Multispectral opto-acoustic tomography of deep-seated fluorescent proteins in vivo. Nat Photon. 2009; 3(7):412–417.
76. Li L, Zemp RJ, Lungu G, Stoica G, Wang LV. Photoacoustic imaging of lacZ gene expression in vivo. J Biomed Opt. 2007; 12(2):020504–3. [PubMed: 17477703]
77. Yao J, Xia J, Maslov KI, et al. Noninvasive photoacoustic computed tomography of mouse brain metabolism in vivo. NeuroImage. 2013; 64:257–266. [PubMed: 22940116]
78. Jin Y, Jia C, Huang S-W, O'Donnell M, Gao X. Multifunctional nanoparticles as coupled contrast agents. Nat Commun. 2010; 1:41. [PubMed: 20975706]
79. Zhang Y, Jeon M, Rich LJ, et al. Non-invasive multimodal functional imaging of the intestine with frozen micellar naphthalocyanines. Nat Nanotechnol. 2014; 9(8):631–8. [PubMed: 24997526]
80. Melancon MP, Zhou M, Li C. Cancer theranostics with near-infrared light-activatable multimodal nanoparticles. Acc Chem Res. 2011; 44(10):947–56. [PubMed: 21848277]
81. Liu Z, Tabakman S, Welsher K, Dai H. Carbon Nanotubes in Biology and Medicine: In vitro and in vivo Detection, Imaging and Drug Delivery. Nano Res. 2009; 2(2):85–120. [PubMed: 20174481]
82. Kumar A, Zhang X, Liang XJ. Gold nanoparticles: emerging paradigm for targeted drug delivery system. Biotechnol Adv. 2013; 31(5):593–606. [PubMed: 23111203]
83. Huynh E, Zheng G. Porphysome nanotechnology: A paradigm shift in lipid-based supramolecular structures. Nano Today. 2014; 9(2):212–222.
84. Hannah A, Luke G, Wilson K, Homan K, Emelianov S. Indocyanine Green-Loaded Photoacoustic Nanodroplets: Dual Contrast Nanoconstructs for Enhanced Photoacoustic and Ultrasound Imaging. ACS Nano. 2013; 8(1):250–259. [PubMed: 24303934]
85. Zanganeh S, Li H, Kumavor PD, et al. Photoacoustic imaging enhanced by indocyanine green-conjugated single-wall carbon nanotubes. J Biomed Opt. 2013; 18(9):096006. [PubMed: 24002193]
86. Morscher S, Driessen WHP, Claussen J, Burton NC. Semi-quantitative Multispectral Optoacoustic Tomography (MSOT) for volumetric PK imaging of gastric emptying. Photoacoustics. 2014; 2(3): 103–110. [PubMed: 25431754]
87. Rhim H, Dodd GD 3rd. Radiofrequency thermal ablation of liver tumors. J Clin Ultrasound. 1999; 27(5):221–9. [PubMed: 10355885]
88. Welch AJ, Motamedi M, Rastegar S, LeCarpentier GL, Jansen D. Laser thermal ablation. Photochem Photobiol. 1991; 53(6):815–23. [PubMed: 1886940]
89. Lal S, Clare SE, Halas NJ. Nanoshell-enabled photothermal cancer therapy: impending clinical impact. Acc Chem Res. 2008; 41(12):1842–51. [PubMed: 19053240]
90. Kim C, Favazza C, Wang LV. In vivo photoacoustic tomography of chemicals: high-resolution functional and molecular optical imaging at new depths. Chem Rev. 2010; 110(5):2756–82. [PubMed: 20210338]
91. Ntziachristos V, Razansky D. Molecular imaging by means of multispectral optoacoustic tomography (MSOT). Chem Rev. 2010; 110(5):2783–94. [PubMed: 20387910]

92. Nie L, Chen X. Structural and functional photoacoustic molecular tomography aided by emerging contrast agents. Chem Soc Rev. 2014; 43(20):7132–70. [PubMed: 24967718]

93. Luke GP, Yeager D, Emelianov SY. Biomedical applications of photoacoustic imaging with exogenous contrast agents. Ann Biomed Eng. 2012; 40(2):422–37. [PubMed: 22048668]

94. Pan D, Kim B, Wang LV, Lanza GM. A brief account of nanoparticle contrast agents for photoacoustic imaging. Wiley Interdiscip Rev Nanomed Nanobiotechnol. 2013; 5(6):517–43. [PubMed: 23983210]

95. Khlebtsov N, Bogatyrev V, Dykman L, et al. Analytical and theranostic applications of gold nanoparticles and multifunctional nanocomposites. Theranostics. 2013; 3(3):167–80. [PubMed: 23471188]

96. Hirsch LR, Stafford RJ, Bankson JA, et al. Nanoshell-mediated near-infrared thermal therapy of tumors under magnetic resonance guidance. Proc Natl Acad Sci U S A. 2003; 100(23):13549–54. [PubMed: 14597719]

97. Wang YW, Xie XY, Wang XD, et al. Photoacoustic tomography of a nanoshell contrast agent in the in vivo rat brain. Nano Lett. 2004; 4(9):1689–1692.

98. Dreaden EC, Alkilany AM, Huang X, Murphy CJ, El-Sayed MA. The golden age: gold nanoparticles for biomedicine. Chem Soc Rev. 2012; 41(7):2740–79. [PubMed: 22109657]

99. Lu W, Melancon MP, Xiong C, et al. Effects of photoacoustic imaging and photothermal ablation therapy mediated by targeted hollow gold nanospheres in an orthotopic mouse xenograft model of glioma. Cancer Res. 2011; 71(19):6116–21. [PubMed: 21856744]

100. Song KH, Kim C, Maslov K, Wang LV. Noninvasive in vivo spectroscopic nanorod-contrast photoacoustic mapping of sentinel lymph nodes. Eur J Radiol. 2009; 70(2):227–231. [PubMed: 19269762]

101. Li P-C, Wang C-RC, Shieh D-B, et al. In vivo photoacoustic molecular imaging with simultaneous multiple selective targeting using antibody-conjugated gold nanorods. Opt Express. 2008; 16(23):18605–18615. [PubMed: 19581946]

102. von Maltzahn G, Park JH, Agrawal A, et al. Computationally guided photothermal tumor therapy using long-circulating gold nanorod antennas. Cancer Res. 2009; 69(9):3892–900. [PubMed: 19366797]

103. Chen YS, Frey W, Kim S, Kruizinga P, Homan K, Emelianov S. Silica-Coated Gold Nanorods as Photoacoustic Signal Nano amplifiers. Nano Lett. 2011; 11(2):348–354. [PubMed: 21244082]

104. Xia Y, Li W, Cobley CM, et al. Gold nanocages: from synthesis to theranostic applications. Acc Chem Res. 2011; 44(10):914–24. [PubMed: 21528889]

105. Wang Y, Black KC, Luehmann H, et al. Comparison study of gold nanohexapods, nanorods, and nanocages for photothermal cancer treatment. ACS Nano. 2013; 7(3):2068–77. [PubMed: 23383982]

106. De la Zerda A, Zavaleta C, Keren S, et al. Carbon nanotubes as photoacoustic molecular imaging agents in living mice. Nat Nanotechnol. 2008; 3(9):557–62. [PubMed: 18772918]

107. Moon HK, Lee SH, Choi HC. In vivo near-infrared mediated tumor destruction by photothermal effect of carbon nanotubes. ACS Nano. 2009; 3(11):3707–13. [PubMed: 19877694]

108. Bianco A, Kostarelos K, Prato M. Applications of carbon nanotubes in drug delivery. Curr Opin Chem Biol. 2005; 9(6):674–9. [PubMed: 16233988]

109. Yang K, Feng L, Shi X, Liu Z. Nano-graphene in biomedicine: theranostic applications. Chem Soc Rev. 2013; 42(2):530–47. [PubMed: 23059655]

110. Chou SS, Kaehr B, Kim J, et al. Chemically exfoliated MoS2 as near-infrared photothermal agents. Angew Chem Int Ed. 2013; 52(15):4160–4.

111. Ku G, Zhou M, Song S, Huang Q, Hazle J, Li C. Copper sulfide nanoparticles as a new class of photoacoustic contrast agent for deep tissue imaging at 1064 nm. ACS Nano. 2012; 6(8):7489–96. [PubMed: 22812694]

112. Zhang Y, Lovell JF. Porphyrins as theranostic agents from prehistoric to modern times. Theranostics. 2012; 2(9):905–15. [PubMed: 23082102]

113. Lovell JF, Jin CS, Huynh E, MacDonald TD, Cao W, Zheng G. Enzymatic regioselection for the synthesis and biodegradation of porphysome nanovesicles. Angew Chem Int Ed. 2012; 51(10): 2429–33.

114. Carter KA, Shao S, Hoopes MI, et al. Porphyrin-phospholipid liposomes permeabilized by near-infrared light. Nat Commun. 2014; 5:3546. [PubMed: 24699423]

115. Jin CS, Lovell JF, Chen J, Zheng G. Ablation of hypoxic tumors with dose-equivalent photothermal, but not photodynamic, therapy using a nanostructured porphyrin assembly. ACS Nano. 2013; 7(3):2541–50. [PubMed: 23394589]

116. Yang K, Xu H, Cheng L, Sun C, Wang J, Liu Z. In vitro and in vivo near-infrared photothermal therapy of cancer using polypyrrole organic nanoparticles. Adv Mater. 2012; 24(41):5586–92. [PubMed: 22907876]

117. Cheng L, Yang K, Chen Q, Liu Z. Organic stealth nanoparticles for highly effective in vivo near-infrared photothermal therapy of cancer. ACS Nano. 2012; 6(6):5605–13. [PubMed: 22616847]

118. Lovell JF, Liu TW, Chen J, Zheng G. Activatable photosensitizers for imaging and therapy. Chem Rev. 2010; 110(5):2839–57. [PubMed: 20104890]

119. Agostinis P, Berg K, Cengel KA, et al. Photodynamic therapy of cancer: an update. CA Cancer J Clin. 2011; 61(4):250–81. [PubMed: 21617154]

120. Ho CJ, Balasundaram G, Driessen W, et al. Multifunctional photosensitizer-based contrast agents for photoacoustic imaging. Sci Rep. 2014; 4:5342. [PubMed: 24938638]

121. Wang S, Huang P, Nie L, et al. Single continuous wave laser induced photodynamic/plasmonic photothermal therapy using photosensitizer-functionalized gold nanostars. Adv Mater. 2013; 25(22):3055–61. [PubMed: 23404693]

122. Terentyuk G, Panfilova E, Khanadeev V, et al. Gold nanorods with a hematoporphyrin-loaded silica shell for dual-modality photodynamic and photothermal treatment of tumors in vivo. Nano Res. 2014; 7(3):325–337.

123. Srivatsan A, Jenkins SV, Jeon M, et al. Gold nanocage-photosensitizer conjugates for dual-modal image-guided enhanced photodynamic therapy. Theranostics. 2014; 4(2):163–74. [PubMed: 24465274]

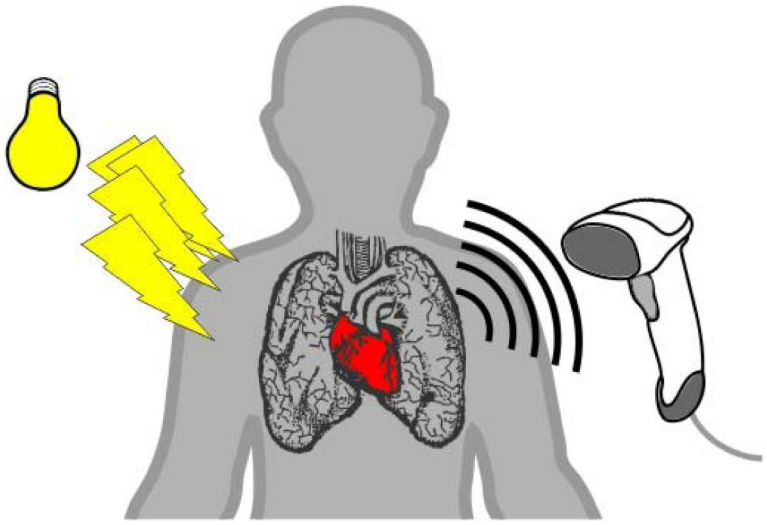

Figure 1.

Fundamental principle of photoacoustic imaging. Pulsed light enters the body as shown on the left side of the image and is detected as photoacoustic waves using ultrasound as it exits the body.

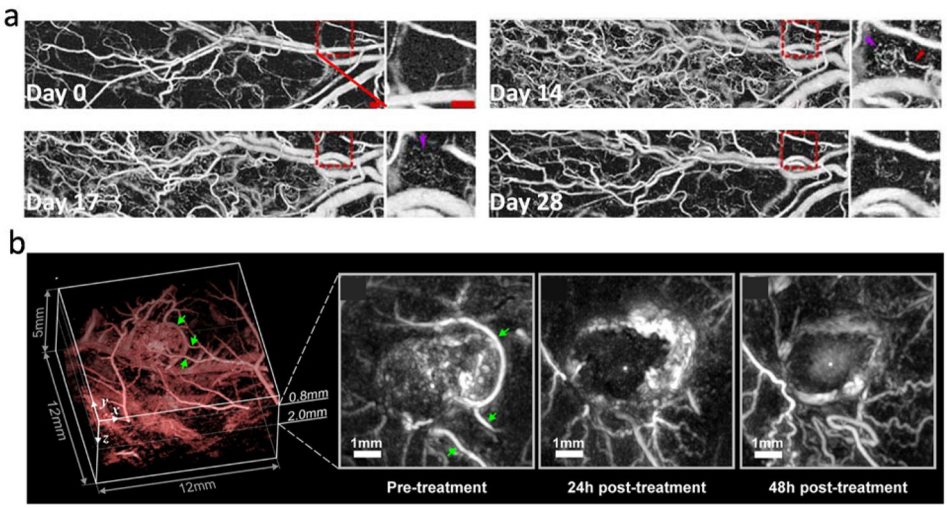

Figure 2.

(a) OR-PAM monitoring of angiogenesis in a transgenic mouse with continual epithelial HIF-1 induction from day 0 to day 14, followed by angiogenic factor withdrawal on day 15. Scale bar: 500 μm. (b) PA images showing the effect of a vascular disrupting agent (OXi4503) on the blood vessel network of a tumor (LS174T) implanted subcutaneously in the flank of a nude mouse. Adapted with permission from [40, 41].

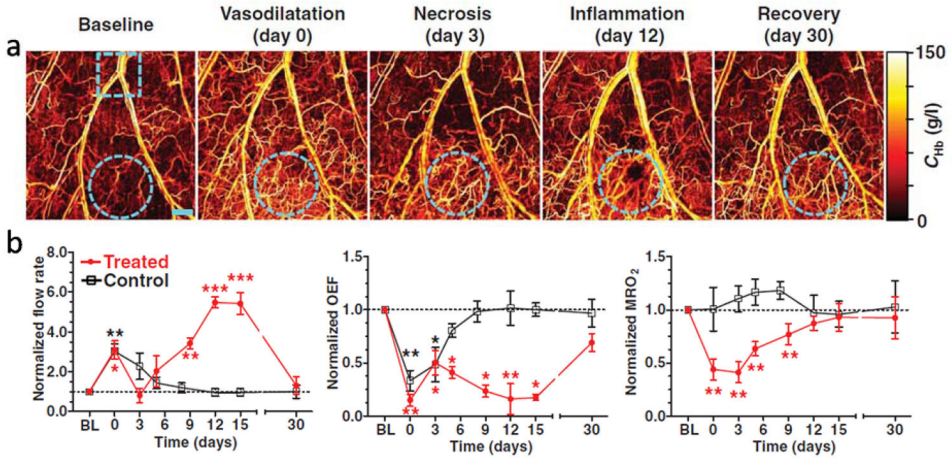

Figure 3.

OR-PAM monitoring of hemodynamic responses after cryotherapy. (a) OR-PAM vasculature images acquired in different phases before and after the application of a liquid nitrogen cryo-probe. The treated area is indicated by cyan dashed circles. Scale bar: 500 μm. (b) OR-PAM quantification of blood flow rate, OEF, and MRO2 within 30 days after treatment. A neighboring area close to the treated region was monitored as a control. Statistics: paired Student's t-test. * $p < 0.05$, ** $p < 0.01$, *** $p < 0.001$, $n = 4$. Data are presented as means ± s.e.m (standard error of the mean). Baseline flow rates: 0.72 ± 0.12 μl/min (treated) and 0.44 ± 0.15 μl/min (control); baseline OEF: 0.35 ± 0.04 (treated) and 0.31 ± 0.05 (control); baseline MRO2: 0.30 ± 0.06 ml/100 g/min (treated) and 0.25 ± 0.07 ml/100 g/min (control). BL: baseline. Adapted with permission from [50].

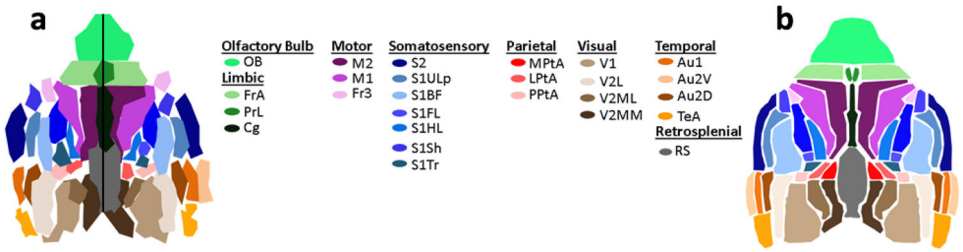

Figure 4.

Functional connectivity map in a live mouse brain, acquired noninvasively by a full-ring array PACT system. (a) Parcellation map of the mouse brain. (b) Corresponding functional regions from the Paxinos histological atlas. The regions and their subregions indicated in the atlas are as follows: Au, auditory cortex; Au1, primary auditory cortex; Au2D, secondary auditory – dorsal area; Au2V, secondary auditory – ventral area; Cg, cingulate; Fr3, frontal cortex area 3; FrA, frontal association; LPtA, lateral parietal association; M1, primary motor cortex; M2, secondary motor cortex; M, motor cortex; MPtA, medial parietal association; OB, olfactory bulb; P, parietal region; PPtA, posterior parietal association; PrL, pre-limbic; RS, retrosplenial area; S1ULp, primary somatosensory – upper lips region; S1BF, primary somatosensory – barrel field; S1FL, primary somatosensory – forelimb region; S1HL, primary somatosensory cortex – hindlimb region; S1Sh, primary somatosensory – shoulder region; S1Tr, primary somatosensory cortex – trunk region; S2, secondary somatosensory; TeA, temporal association cortex; V1, primary visual cortex; V2, secondary visual cortex; V2MM, secondary visual cortex – mediomedial region; V2ML, secondary visual cortex – mediolateral region; and V2L, secondary visual cortex – lateral region. Reproduced with permission from [60].

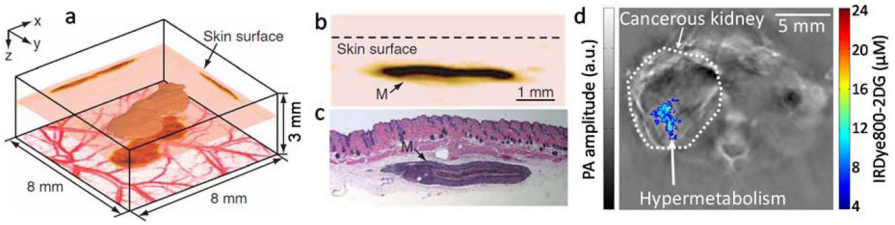

Figure 5.

(a)–(c) *In vivo* imaging of a subcutaneously inoculated B16-melanoma in a nude mouse. (a) Three-dimensional rendering of the melanoma from the data acquired at 764 nm. A composite of two maximum amplitude projection (MAP) images (acquired at 584 nm and 764 nm, respectively) projected along the z axis is shown at the bottom. The top surface of the tumor is 0.32 mm below the skin surface, and the thickness of the melanoma is 0.3 mm. (b) An enlarged cross-sectional image of the melanoma parallel with the z-x plane. (c) Hematoxylin-and-eosin stained section at the same marked location. M, melanoma. (d) *In vivo* cross-sectional image of a mouse with orthotopically implanted 786-O kidney tumor, acquired using the full-ring array PACT system. IRDye800-2DG concentration is overlaid in color on the anatomical image (gray). Adapted with permission from [62, 64].

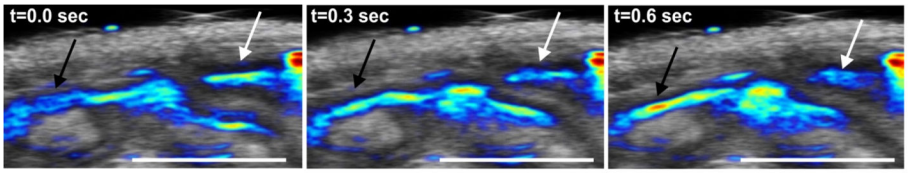

Figure 6.

Functional intestinal real-time imaging in mice. PA signal generated by nanonap contrast agent is shown in color with ultrasound overlaid in gray. Image shown is a transverse plane. The black arrow shows nanonap inflow while the white arrow shows outflow. 5 mm scale bars are indicated. Adapted with permission from [79].

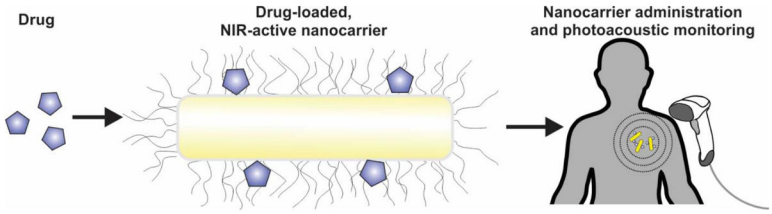

Figure 7.

Using NIR-active nanocarriers to track drug delivery. A drug can be loaded onto drug delivery vehicles, in this case a PEGylated gold nanorod. The administered drug can then be indirectly monitored by monitoring the nanocarrier using PAI. Since this techniques examines the nanocarrier, the association between the drug and nanocarrier should be sufficiently stable in vivo.